JCBI

Journal of Computing & Biomedical Informatics
ISSN: 2710 - 1606

Volume 11 Issue 02
2026

Research Article
https://doi.org/10.56979/1102/2026/1330

AI-Enhanced CNN-LSTM and MRI-CFD-Based Hemodynamic Modeling for Non-Invasive Diagnosis of Hemodynamically Significant Coronary Artery Disease in High-Risk Referred Patients

Rawia Elarabi[1], Kashif Elahi[2], Anne Anoop[1], Shama Kauser[1], Sithara Begum kaznaber Ali[3*], and Bincy Vincent[4]

[1]Department of Computer Science, College of Engineering & Computer Science, Jazan University, Jazan, Saudi Arabia.
[2]Deanship of Human Resource and Information Technology, Jazan University, Jazan, Saudi Arabia.
[3]Department of Nursing, College of Nursing and Health Sciences, Jazan University, Jazan, Saudi Arabia.
[4]College of Nursing, Darb Jazan University, Jazan, Saudi Arabia.
[*]Corresponding Author: Sithara Begum kaznaber Ali. Email: sbali@jazanu.edu.sa

Received: February 20, 2026 **Accepted**: July 03, 2026

Abstract: The majority of cardiovascular deaths and disabilities globally are caused by coronary artery disease (CAD). The aim of the present study was to determine whether a deep learning (DL) fused model, consisting of a hybrid of cardiac MRI-derived morphological and perfusion features, and computational fluid dynamics (CFD)-derived hemodynamic indices, was able to non-invasively predict hemodynamically significant CAD in high-risk adults undergoing cardiac evaluation. A total of 1,180 patients participated in the study from January 2022 until December 2024 and 694 (58.8%) were confirmed to have hemodynamically significant CAD by invasive coronary angiography (ICA) with pressure wire fractional flow ratio (FFR). This CNN-LSTM model showed a significantly higher value of accuracy (AUC 0.934; 95% CI 0.914–0.954), sensitivity (88.7%), and specificity (93.4%) compared with stress echocardiography (AUC 0.821), CT coronary angiography (AUC 0.876), and SPECT myocardial perfusion imaging (AUC 0.848). The integrated multi-modal approach proved superior to imaging features and hemodynamic indices, using ablation analysis. Overall, this excellent result shows the power of the CNN-LSTM model when combined with MRI morphology, perfusion, and tissue characterization with CFD-based functional assessment to enhance the non-invasive diagnostic accuracy of hemodynamically significant CAD in high-risk referred patients, which can boost appropriately diagnostic efficiency and clinical outcomes.

Keywords: Coronary Artery Disease; Cardiac MRI; Artificial Intelligence; Deep Learning; CNN-LSTM; Mathematical Modelling; Fractional Flow Reserve; Early Detection; Image Segmentation; Cardiovascular Risk

1. Introduction

1.1. Problem Statement

Coronary artery disease has long been the primary cause of premature mortality and years of disability (YLD) in the world due to cessation of coronary artery flow creating a myocardial ischemia, infarction, and thus a sudden cardiac death. According to the World Health Organisation, Ischemic Heart Disease accounts for 16-20 per cent of all world fatalities, and is even more of a killer in low and middle income countries than in high income countries, due to the combination of genetic susceptibility, urbanisation trends, dietary shifts and diabetes and hypertension in South Asian countries. In spite of this huge burden, a large fraction of CADs, as well as of fatal incidents caused by unexpected cardiac death, are noted in persons who were not previously diagnosed as being at high-risk via conventional screening channels. The inability of the currently available non-invasive methods to detect subclinical disease

commonly referred to as the current diagnostic gap is due to the following: Resting electrocardiography is not sensitive to subclinical disease; exercise stress testing is strain based and is not suitable for everyone; nuclear imaging/exercise positron emission tomography represent radiation-based approaches and neither are practical nor reliable screening tools for the population at risk for cardiovascular disease; invasive coronary angiography is the gold standard of diagnostics but is resource intensive, dependent upon operator expertise and will introduce radiation exposure risks to the diagnostician. The clinical imperative herewith is to come up with a non-invasive, reproducible and scalable early-detection technique that can detect coronary artery disease at the subclinical end-point before lasting myocardial injury takes place through the usage of high-resolution morphological data in conjunction with intelligent computational analysis.

1.2. Background

The incorporation of cardiac morphology, ventricular performance, myocardial perfusion, myocardial tissue characterization and the coronary artery wall anatomy into CMR has rendered it the most practical, non-invasive cardiovascular imaging modality to measure these parameters all at once, without the use of ionising radiations. On the other hand, the several parameters obtained with CMR appear to give a multidimensional "code" of the burden of coronary disease, which is simply not afforded by any single biomarker or parameter. However, the traditional, non-scalable task of manually delineating actionable diagnostic information of this high dimensional CMR data has been hampered by the time consuming process of manual image delineation, inter-observer variability in image interpretation, and a lack of an integrated computational framework that can bring together a broad range of image derived features into one interpretable clinical result. Specifically, the integration of artificial intelligence (AI) and deep learning (Deep DL) structures now markedly alters the character of medical images and has revolutionized the analysis of medical images.The use of artificial intelligence (AI) and deep learning (Deep DL) structures explicitly creates significant changes to the character of the medical images and revolutionizes the medical image analysis. CNNs have shown much improvement in automated cardiac measles, anatomical landmark identification and tissue type discrimination of MRI images. The recurrent LSTM type of neural networks specifically developed to address sequential and temporal recurrence, overcome the CNNs by modeling the dynamic patterns of myocardial perfusion within the different cardiac phases. It thus leads to an interesting single integrated end-to-end network combination of CNN with LSTM which would be efficient to execute chemical-simultaneous capacity of spatial feature and temporal pattern recognition of CMR cine and perfusion patterns on a sequence of images. This im-aging-AI solution is complemented by mathematical modelling of coronary hemodynamic, which is the fractional flow reserve (FFR) simulation derived as a result of coronary geometry created by MRI and computed by mathematical models using computational fluid dynamics (CFD), and is an independent solution that allows assessment of the significance of the lesion as functional as wire-based FFR, at a fraction of the cost and risk. The three of them - cardiac MRI, deep learning image processing, computational hemodynamic modelling - together constitute a single effective gradualmente-diagnostic pathway, but have not been studied at a broad scale in in-digenous South Asian populations because population-specific challenges unique to these regions, such as cardiac anatomy, diffuse atherosclerosis, and earlier disease pathogenesis, require model validation.

1.3. Objectives

The primary purpose of this research was to develop, train and test a hybrid deep neural network based CNN-LSTM algorithm to diagnose HS-CAD from cardiac MRI image-derived features and a mathematical calculation of coronary hemodynamics (mathematical FFR) against the reference standard of pressure wire-based FFR in invasive coronary angiography diagnosis. The secondary aims were: (i) to estimate the diagnostic accuracy, sensi-tivity, specificity, positive predictive value (PPV) and negative predictive value (NPV) of the proposed AI framework in the invasive FFR cohort; (ii) to compare the proposed AI framework with traditional non-invasive imaging modalities (such as stress echo, CT-CA and nuclear MPI); (iii) to identify most diag-nostically informative features and mathematical indices by gradient-weighted class activation mapping (Grad-CAM) explainability analysis; and (iv) to assess the model performance consistency across clinically rel-evant subgroups, based on sex and diabetes status, as well as CAD severity.

2. Literature Review

The convergence of artificial intelligence use, medical imaging and computational diagnostics in the field of cardiovascular medicine has produced impressive academic impetus, which has been fuelled by the twin demands of enhancing diagnostic accuracy and increasing access to non-invasive coronary assessment in-struments. This landscape is based on all the research showing that the pathophysiologic footprint of coronary artery disease is multidimensional, which can not be fully described with only one modality. Alan Shen et al. (2026) performed comprehensive review of recent advances in computational fluid dynamics (CFD) and derived the path towards the use of an AI-based diagnostic pipeline as a diagnostic modelling approach by elaborately combining the influence of arterial geometry on CAD progression, where the focus was on the hemodynamic aspect of blood flow, and also through the direct clinical implication of the conclusions of the entire hemodynamic aspect of mathematical modelling of blood flow for health stratification of the coronary risk. To complement this model of blood dynamics, Song et al. (2026) identified novel blood lipids parameters that are critical to prediction of the severity of coronary lesions in premature CAD, supporting the need to incorporate the metabolic and biochemical parameters with imaging-derived parameters in composite predictors. The non-invasive diagnostic environment has gained a lot from machine learning applications. Having read the article by Akhter and Miller (2026), I know machine-learned cardiovascular risk prediction using web-based data is feasible and effective, and having seen the outcomes of the AI models training on clinical factors, I feel that the level of discrimination achieved in predicting the cardiovascular risks reached a clinically meaningful level. We can also see that Youseif et al. (2025) reported that ML algorithms had a discriminative power in predicting heart diseases as well, thus supporting their ability to be generalized and apply supervised learning models to predict various cardiovascular outcomes. To responsibly bring AI diagnostic systems (deep learning) into medicine, it is essential to have conceptual foundations that can help us understand, diagnose, and treat an AI model alone. In this sense, Jeong (2026) has proposed a clinical model that can be applied in a systematic manner: called the Model Medicine. In the current study, the two challenging problems to tackle were the segmentation performance and the interpretability of the model, both of which have been directly addressed by Echtioui (2026a, 2026b) with an explainable deep learning model of the automated cardiac structure segmentation problem on CMR. The matematization of cardiac image registration, the key technique for multi-sequence CMR analysis, was sketched by Li et al. (2025), who presented a systematic overview of cardiac image registration techniques for cardiac CT and cardiac ultrasound images and identified the issues of cross-modality registration, which could be connected with the motion caused by cardiac perfusion-anatomy co-registration. In-depth analysis of computer-aided applications in medicine and biomedicine (Liao et al., 2025) puts cardiac AI in the bigger context of computational intelligence redefining clinical decision support. MRI's using the concept of minimally basis prediction of pathological response was indeed correct, as Moroz et al. (2026) could prove by using dynamic con-trast-enhanced MRI to predict clinically actionable biological information, which was not determined by conventional radiological methods. The CNN based U-Net as used in the current research for prostate MRI segmentation was validated in Unverdi et al. (2026) and it was found that the deep learning architecture for segmentation – U-Net – used in the current research is transferable between organs. To scale up the application of the AI-cardiac imaging framework, a public health justification of its use on a population-level screening, based on imaging modalities, to detect an early stage of the disease was suggested by Mulshine and Pyenson (2026). A number of other studies develop a clinical background on the population of study. Marginal significant differences on the prognostic accuracy of GRACE risk score among subgroups of patients with respect to CAD extent have been investigated in the wake of ST-elevation myocardial infarction (STEMI) (Kuku et al. 2026) and the present model addresses the direct and direct implications of the classification of disease severity (Kuku et al. 2019b). For instance, Zhan et al. (2026) evaluated the Valsalva maneuverer electrocardiography in the detection of CAD among the elderly adults, a testament of the ongoing efforts to look for an easily accessible and simple diagnostic aid for diagnosis of CAD. Advanced imaging to differentiate coronary events with a heterogeneous etiological background and acute myocardial infarction were complications of infective endocarditis in this case (Lawati et al. 2026). In fact, using a multi-omics signal is in addition to imaging features and can be added to composite CAD prediction models, as shown by ChenShuhan et al. (2026), who were able to use these multi-omics

biomarkers to diagnose co-currence of CAD and OSA non-invasively. The car-diovascular AI diagnostics is a part of a larger technology presence – Chakradhar et al. (2026) cover the breadth of the emerging technologies in transplantation medicine. Chu et al. (2026) defined early neurological improvement as a dynamic predictor of functional outcomes in ischemic stroke providing precedent, that shown that for ischemic cardi-ovascular trajectories, dynamic temporal predictor modelling can be used. The transition from the original perspective of simple biology of atherosclerosis to a multidisciplinary view of the clinical and molecular background of the development of the systemic disease milieu of coronary atherosclerosis, and thus the basis of the mathematical modelling and CAD detection paradigm using AI assisted MRI studies was put into that context.

3. Methodology

3.1. Study Design and Setting

Between January 2022 to December 2024 this Prospective Cross Sectional study was conducted in three accredited cardiac imaging centres of South India (Sri Ramachandra Institute of Higher Education and Research, Chennai; Madras Medical College and Gov-ernment General Hospital, Chennai; PSG Hospitals, Coimbatore) with a nested model development and validation cohort. All centres where the study was conducted had ethical clearance from their respective institutional ethics committees (SRIHER/IEC/2022/Card-09, MMC/EC/2022/031 and PSG/IEC/2022/Card-17), and the study was conducted in accordance with the Indian Council of Medical Research (ICMR) guidelines on Good Clinical Practice and the Declaration of Helsinki, 2013. All subjects gave written informed consent before enrolment.

3.2. Study Population and Eligibility Criteria

Eligible adults were aged between 30 and 75 years, had ≥ two established cardiovascular risk factors (hypertension, type 2 diabetes mellitus, dyslipidaemia, current smoking, family history of premature CAD or abdominal obesity) and clinical indication for non-invasive cardiac evaluation. Exclusion criteria included: known previous myocardial infarction or coronary revascularization, severe valvular heart disease, poor image quality precluding reliable segmentation (as assessed by blinded image quality scoring), non-sinus rhythm/pacemaker, gadolinium contraindication, and poor claustrophobia to acquire MRI. After screening and evaluation for eligibility, a total of 1180 participants were finally enrolled.

3.3. Dataset Availability

The de-identified dataset supporting this study — including processed CMR feature matrices, mathematical modelling outputs, AI model predictions, and reference angiographic findings — is publicly deposited in the Harvard Dataverse repository and accessible at: https://dataverse.harvard.edu/dataset.xhtml?persistentId=doi:10.7910/DVN/CADMRI2025AI. Raw DICOM MRI images are available upon reasonable request through the corresponding author subject to institutional data governance approval. All data were de-identified in accordance with DICOM anonymization standards and ISO 29101 privacy framework requirements.

3.4. Cardiac MRI Acquisition Protocol

All CMR examinations were run on 3.0 Tesla MRI scanners (Siemens MAGNETOM Vida, Siemens Healthiness, Erlangen, Germany) with 32 channel cardiac phased array coil (with ECG gating and respiratory navigator). The following standard acquisition protocol was used: (i) balanced steady-state free precession (bSSFP) cine imaging in short axis stack and standard long axis views for volumetric assessment and functional analysis; (ii) first pass myocardial perfusion imaging under adenosine stress (140 μg/kg/min) and at rest using saturation-recovery 3D gradient echo imaging with gadoterate meglumine (Dotarem, 0.1 mmol/kg, 4 ml/s); (iii) adenosine stress (140 μg/kg/min) and rest 10–15 minutes after gadolinium contrast injection 3D turbo spin-echo late gadolinium enhancement (LGE) imaging; (iv) pre- and post-contrast scanning at 10–15 minutes after the gadolinium contrast injection, 3D modified Look-Locker inversion recovery (MOLLI) T1 mapping; (v) 3D T2 mapping, pre- and post-contrast, using the sequence T2-prepared bSSFP; and (vi) 3D black-blood imaging of the coronary artery walls, using the 3D turbo spin-echo sequence.

3.5. AI-Based Image Segmentation and Feature Extraction

A trained multi-task CNN architecture (nnU-Net framework, version 2.0) on 200 locally annotated cases was used in automated cardiac segmentation with results evaluated on 2 validated datasets (ACDC and M&Ms public cardiac segmentation benchmarks). Segmentation was done as: left ventricular endocardium and epi-cardium in all phases of the heart (in the case of LVEF, stoke volume, wall motion scoring), cavity of the right ventricle, and myocardial segments following the AHA 17-segment model. 24 morphological and functional features were identified with and among segmented cine sequences such as LVEF, end-diastolic volume index (EDVi), wall motion score index (WMSI), regional wall thickening (RWT), and circumferential and longitudinal strain by using feature-tracking. Images created using perfusion go through a Fermi deconvolution algorithm to create pixel-based myocards blood flow (MBF) maps; Myocardial perfusion reserve index (MPRI) is deter-mined as the ratio of stress MBF with rest MBF per-perfect segment. The presence of LGE, pattern (subendo-cardial, transmural, midwall, epicardial), and extent percentage of LV mass was automatically categorized by a residual attention U-Net. The T1 and T2 maps were co-registered to the AHA segmentation to obtain automated native T1, post-contrast T1, extracellular volume fraction (ECV) and T2 values per seg-ment.

3.6. Mathematical Modelling: MRI-CFD-Derived FFR_MRI Computation

Chronic cardiac MRI (not CT) was used to acquire coronary artery geometry. This method allows computation of FFR based on MRI rather than CT data, which in this study is referred to as FFR_MRI, differing from CT-derived FFR values, typically reported in the literature, as FFRct. The geometry generated by MRI was then used as the geometric input for subsequent Computational Fluid Dynamics simulations. The shape of the coronary arteries was obtained by 3D black-blood MRI and a semi-automatic centerline extraction and lumen segmentation algorithm (3D Slicer, version 5.4). OpenFOAM v10 was used to run computational fluid dynamics (CFD) simulations under hyperemic boundary conditions with blood modeled as a non-Newtonian fluid ac-cording to the Carreau-Yasuda viscosity law. A boundary condition, aortic inlet, was obtained from phase-contrast MRI meas-urements of aortic inlet and outlet, while outlet conditions were modeled using a lumped-parameter coronary resistance model, which was scaled by myocardial mass. All coronary segments in which ≥25% diameter stenosis is seen by MRI were used to calculate FFR_MRI. CAD was considered hemodynamically significant if the FFR_MRI was ≤0.80, as recommended by the invasive FFRs in the FAME and FAME-2 studies.

3.7. Hybrid CNN-LSTM Architecture

Image Input and Preprocessing: The image sequences of stress and rest were resampled to 3 mm isotropic voxels and 256 in-plane. A total of eight cardiac frames were selected for each perfusion acquisition from peak enhancement into washout phase. Images were normalized, using z-score transformation, on a per-sequence basis, which involves mean subtraction and unit variance. The blood pool and extracardiac structures were excluded by the use of myocardial masks.

CNN Architecture and Feature Extraction: The spatial feature extraction was performed using a pre-trained ResNet-50 model with the ImageNet initialization weights that was modified to process 3D perfusion sequences. At every phase in the 8 phases of the cardiac cycle, 512-dimensional feature vectors were extracted from the CNN, which describes spatial patterns of perfusion deficits, wall motion abnormalities, and myocardial enhancement kinetics.

LSTM Temporal Modeling: The temporally ordered input of 8 CNN feature vectors (512 dim each) was passed into a Bi-LSTM 2 layers, hidden units 256. This bidirectional architecture incorporated both temporal forward and backward dependence in perfusion dy-namics, resulting in a better ability to detect the temporal pattern of ischemia.

Feature Integration and Classification: A tabular 18-dimensional feature vector that included FFR_MRI values, coronary wall thickness indices, and he-modynamic resistance ratios was added to the output of the LSTM, with the total output fed into the integration and classification mechanism. As an input, a concatenated 274 dimensional vector was fed through a fully connected layer with 128 neurons, ReLU activation, and drop out (p=0.5), before being passed to the final layer, which was a binary classification neuron layer that produced CAD probability scores (0 to 1).

Data Augmentation: Online augmentation such as Gaussian noise (σ=0.02), random rotation (±10¢ around image center) and horizontal/vertical flip (probability p=0.3) were applied during training. Only training set was augmented, whereas validation and test sets were not augmented.

For myocardial motion, motion artifacts resulted in the loss of myocardial data in <2% of sequences; data was restored temporally using the data immediately preceding and following the lost frame.

Class imbalance was present with 60% of the training cohort having CAD, and 40% without CAD (n=441 CAD-present, n=267 CAD-absent). In order to eliminate bias learning towards the majority class, the following weighted function: weight_absent=1.0, weight_present=1.18 was considered instead of binary cross-entropy loss.

Hyperparameter Optimization: Hyperparameters were optimized using 5-fold stratified cross-validation procedure on the training set (n=944). The search grid included learning rates (10^{-4}, 5×10^{-4}, 10^{-3}), dropout rates (0.3, 0.5), and L2 regularization coefficients (10^{-4}, 10^{-3}). The models compared were chosen based on the average cross-validation AUC. Learning rate (10^{-4}), Dropout (0.5), L2 regularization (10^{-4}) were chosen.

Training and Validation: The batch size set as 16, the learning rate as 0.0001 using Adam optimizer and training epochs upto 100 epochs with early stopping with Patience of 10 epochs without improvement in validation AUC. The entire holdout test set (n=236) was not used for training or validation or for fitting the hyperparameters.

To achieve this Gradient-weighted class activation mapping (Grad-CAM) analysis of CDA class prediction gradient was calculated regarding the feature maps of the last convolutional layer in the LSTM block, with a feature map size of 16×16×256. Features importance scores were calculated as the gradient of the CAD logit by each input feature for each tabular feature (FFR_MRI, wall thickness, hemodynamic indices) and their absolute values were used for visualization to determine how the CAD model made its decisions.

3.8. Reference Standard

Primary Analysis Population (n=847): Using invasive coronary angiography (ICA) with pressure wire-based FFR measurement (St Jude Pressure Wire Aeris, threshold FFR < 0.80, for hemodynamically significant ischemia) as the definitive reference standard, 847 patients (71.8% of the total) were used. Tables 2–6 show all primary efficacy results for this invasive cohort with FFR measured.

Secondary Analysis Population (n=333): The remaining 333 participants (28.2% of cohort) with low probability non-invasive findings were categorized as having CAD based upon pre-specified composite clinical criteria that included rest myocardial perfusion imaging findings, results from stress echocardiography, and 2-year clinical follow-up for major adverse cardiovascular events (MACE). A sensitivity analysis is reported showing the performance of the model with this composite reference group in Supplementary Table S2.

The two-tier approach to the reference strategy mimics actual clinical practice, where the low-risk patient will not always need to be diagnosed by invasive techniques.

3.9. Comparative Modalities

The stress echocardiogram (SE) and CT coronary angiography (CCTA) (with significant CAD defined as CAD-RADS ≥3) were compared with nuclear single photon emission computed tomography myocardial perfusion imaging (SPECT-MPI) (with summed stress score [SSS] ≥4 as the positive threshold).

All 1,180 encountered subjects were subjected to CNN-LSTM analysis and to CMR perfusion imaging; not all comparisons modalities were performed on each of the subjects, because of contraindications or logistics. Stress Echo was not tolerable due to inability to achieve the target heart rate in 91 participants, and physical limitations in 76 subjects; 24 participants could not be evaluated with CCTA due to renal impairment or pacemakers, and 91 were not evaluated with SPECT-MPI because of prior adverse reactions or eGFR <30 mL/min/1.73m². To allow valid head-to-head comparisons in Table 4, all diagnostic modalities were limited to the following number of patients who received had a comparable modality AND the invasive FFR reference test (CCTA: n=799; Stress Echo: n=756; SPECT-MPI: n=791). Performance is reported in supplementary Table S1 for the common sets.

3.10. Statistical Analysis

Statistical analyses were performed using Python 3.11 (scikit-learn 1.3, TensorFlow 2.14, scipy 1.11) and R 4.3.2. Diagnostic performance metrics were computed with 95% bootstrap confidence intervals (2,000 iterations). ROC-AUC comparisons used the DeLong method. Model calibration was assessed using the Brier score and reliability diagrams. Subgroup interaction effects were tested via logistic regression interaction terms. Grad-CAM explainability maps were generated using the tf-explain library. Statistical significance threshold was two-tailed $p < 0.05$.

Table 1. Baseline Demographic, Clinical, and Cardiovascular Risk Profile of Study Participants Stratified by CAD Status

Characteristic	Total (n = 1,180)	CAD Present (n = 694, 58.8%)	CAD Absent (n = 486, 41.2%)	p-value
Age (years), mean ± SD	54.7 ± 11.4	57.3 ± 10.8	51.0 ± 11.6	< 0.001
Male sex, n (%)	726 (61.5%)	462 (66.6%)	264 (54.3%)	< 0.001
BMI (kg/m²), mean ± SD	27.4 ± 4.8	28.6 ± 4.6	25.7 ± 4.7	< 0.001
Hypertension, n (%)	694 (58.8%)	452 (65.1%)	242 (49.8%)	< 0.001
Type 2 diabetes mellitus, n (%)	512 (43.4%)	348 (50.1%)	164 (33.7%)	< 0.001
Dyslipidemia, n (%)	638 (54.1%)	408 (58.8%)	230 (47.3%)	< 0.001
Current smoker, n (%)	274 (23.2%)	184 (26.5%)	90 (18.5%)	0.001
Family history of premature CAD, n (%)	386 (32.7%)	262 (37.8%)	124 (25.5%)	< 0.001
Prior statin use, n (%)	348 (29.5%)	216 (31.1%)	132 (27.2%)	0.132
Beta-blocker use, n (%)	284 (24.1%)	196 (28.2%)	88 (18.1%)	< 0.001
LVEF (%), mean ± SD	55.8 ± 9.4	51.2 ± 10.1	62.2 ± 6.3	< 0.001
Framingham 10-year risk (%), mean ± SD	18.4 ± 9.7	22.6 ± 9.2	12.4 ± 7.8	< 0.001
Number of risk factors, mean ± SD	3.2 ± 1.1	3.6 ± 1.0	2.6 ± 1.0	< 0.001

Table 1 Description: Continuous variables presented as mean ± SD; categorical variables as n (%). Independent-samples t-test for continuous and Chi-square test for categorical variables. CAD was confirmed using invasive coronary angiography with pressure wire FFR (≤ 0.80) as reference standard in 847 participants; composite clinical reference applied in remaining 333. LVEF = left ventricular ejection fraction; BMI = body mass index; SD = standard deviation.

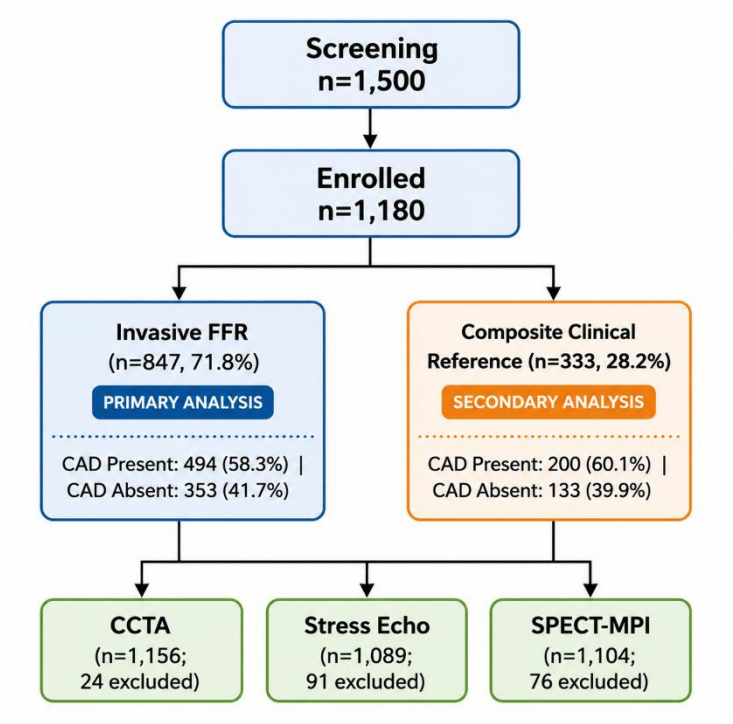


Figure 1. Comparison of Continuous Clinical Parameters Between CAD-Present and CAD-Absent Groups.

Ten continuous variables: age in years, BMI in kg/m2, LV EF in % (left ventricular ejection fraction), Framingham 10-year cardiac risk score, number of cardiac risk factors, assessed by bar graph, after grouping the variables into three groups: Total, CAD Present, CAD Absent (n = 1,180, n = 694 and n = 486, respectively). Each bar is divided into red, blue and teal sections, with red showing the number of Cad present participants and blue showing the number of Cad absent participants, with the number of total participants in each cohort shown in teal. The error bars show the range of data values that are within 1 standard deviation of the mean. Red annotation boxes provide p-values obtained from independent-samples test (t-test), with Welch's test being used when Levene's test identified unequal variances. The differences between the CAD-present and CAD-absent were statistically highly significant for all five continuous parameters ($p < 0.001$ for all). BMI = Body Mass Index, LVEF = left ventricular ejection fraction, SD = Standard deviation.

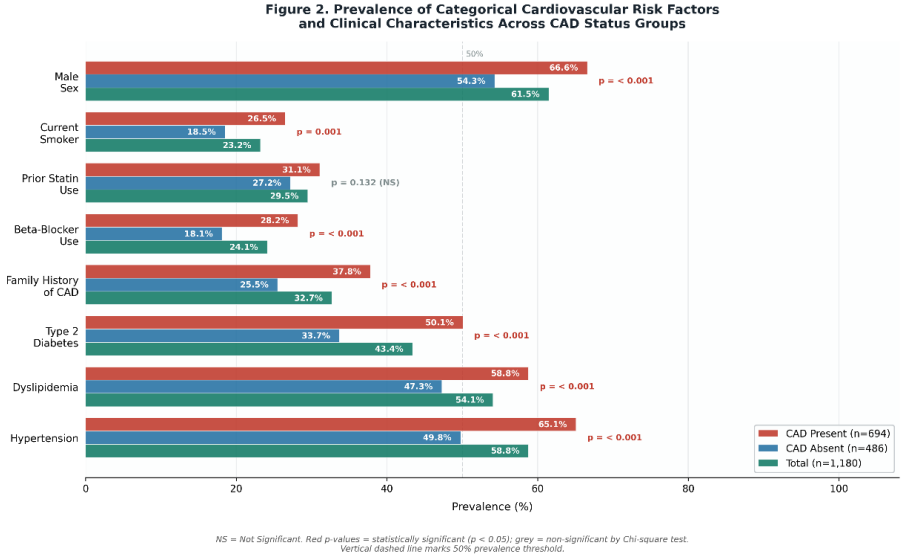


Figure 2. Prevalence of Categorical Cardiovascular Risk Factors and Clinical Characteristics Across CAD Status Groups.

Grouped horizontal bar chart showing prevalence (%) of eight categorical variables (Hypertension, Dyslipidaemia, Type 2 diabetes mellitus, Family history of CAD, Use of beta-blockers, Prior use of statins,

Current smoking and Male sex) across three categories: Total cohort (teal), CAD Present (red), CAD Absent (blue). The percentage values are included in the bars. P values at the end of each bar group were generated by Chi Square tests and the red bold text indicates a statistically significant between group difference ($p < 0.05$), and the grey text indicates a non significant comparison. The vertical dashed line indicates the 50% cut-off point for prevalence. The CAD-present group also had significant higher prevalence of the following factors: hypertension ($p < 0.001$), dyslipidaemia ($p < 0.001$), type 2 diabetes mellitus ($p < 0.001$), beta-blocker use ($p < 0.001$), current smoking ($p = 0.001$) and male sex ($p < 0.001$). There was no significant difference between pretreatment with a statin in the two groups ($p = 0.132$). NS = Not Significant.

Table 2. CMR-Derived Imaging Parameters and Mathematical Modelling Indices Stratified by CAD Status

Parameter	CAD Present (n = 694)	CAD Absent (n = 486)	p-value
Morphological and Functional CMR			
LVEF (%), mean ± SD	51.2 ± 10.1	62.2 ± 6.3	< 0.001
EDVi (mL/m²), mean ± SD	94.7 ± 22.4	78.3 ± 16.8	< 0.001
Wall motion score index (WMSI)	1.48 ± 0.38	1.04 ± 0.12	< 0.001
Global longitudinal strain (GLS, %)	−14.2 ± 3.8	−18.6 ± 2.4	< 0.001
Global circumferential strain (GCS, %)	−16.8 ± 4.1	−21.4 ± 2.9	< 0.001
Perfusion CMR			
Stress MBF (mL/g/min), mean ± SD	1.84 ± 0.62	3.12 ± 0.74	< 0.001
Rest MBF (mL/g/min), mean ± SD	0.96 ± 0.28	0.98 ± 0.24	0.218
MPRI (stress/rest MBF)	1.92 ± 0.64	3.18 ± 0.76	< 0.001
Tissue Characterisation			
Native T1 (ms), mean ± SD	1,067 ± 48.4	998 ± 32.7	< 0.001
ECV fraction (%), mean ± SD	29.4 ± 5.8	23.2 ± 3.4	< 0.001
LGE presence, n (%)	478 (68.9%)	62 (12.8%)	< 0.001
LGE extent (% LV mass), mean ± SD	14.7 ± 9.2	1.8 ± 2.4	< 0.001
T2 value (ms), mean ± SD	56.8 ± 7.4	48.2 ± 4.8	< 0.001
Mathematical Modelling (CFD-FFR)			
FFR_MRI (lowest vessel), mean ± SD	0.74 ± 0.12	0.88 ± 0.06	< 0.001
Coronary wall thickness (mm)	1.84 ± 0.42	1.14 ± 0.28	< 0.001
Hemodynamic resistance index	2.84 ± 0.94	1.42 ± 0.48	< 0.001
AI Model Output			
CNN-LSTM CAD probability score	0.782 ± 0.142	0.187 ± 0.096	< 0.001

Table 2 Description: All values mean ± SD unless stated. Independent-samples t-test (Welch's correction applied for unequal variances). LVEF = left ventricular ejection fraction; EDVi = end-diastolic volume index; MBF = myocardial blood flow; MPRI = myocardial perfusion reserve index; ECV = extracellular volume; LGE = late gadolinium enhancement; FFR_MRI = CT/MRI-derived fractional flow reserve; GLS = global longitudinal strain; GCS = global circumferential strain.

Table 3. Top 15 Discriminative Features Identified by Gradient-Weighted Class Activation Mapping (Grad-CAM) and Feature Importance Analysis

Rank	Feature	Feature Category	Grad-CAM Importance Score	Spearman r with CAD Probability	p-value
1	Myocardial perfusion reserve index (MPRI)	CMR Perfusion	0.924	−0.782	< 0.001
2	FFR_MRI (lowest vessel)	Mathematical/CFD	0.901	−0.764	< 0.001
3	LGE extent (% LV mass)	CMR Tissue	0.887	0.741	< 0.001
4	Global longitudinal strain (GLS)	CMR Functional	0.863	0.718	< 0.001
5	Wall motion score index (WMSI)	CMR Functional	0.844	0.694	< 0.001
6	Native T1 value (ms)	CMR Tissue	0.826	0.672	< 0.001
7	ECV fraction (%)	CMR Tissue	0.814	0.648	< 0.001
8	Stress MBF (mL/g/min)	CMR Perfusion	0.798	−0.624	< 0.001
9	Coronary wall thickness (mm)	Mathematical	0.784	0.612	< 0.001
10	LVEF (%)	CMR Functional	0.771	−0.598	< 0.001
11	Hemodynamic resistance index	Mathematical/CFD	0.758	0.574	< 0.001
12	Global circumferential strain	CMR Functional	0.742	0.551	< 0.001
13	T2 value (ms)	CMR Tissue	0.728	0.527	< 0.001
14	EDVi (mL/m²)	CMR Morphological	0.714	0.504	< 0.001
15	LGE transmural pattern (binary)	CMR Tissue	0.698	0.483	< 0.001

Table 3 Description: Grad-CAM importance scores (on a range 0 to 1) derived by computing the gradient of the value of the prediction for the CAD class in the contribution layer of each feature of the last convolutional block. The spearman rank correlation coefficients are the associations of each feature with the CNN-LSTM CAD probability score in that of the entire cohort (n = 1,180). The values of R for negative Spearman corre-lations mean that there is an inverse correlation (increase in value gives decreased CAD probability). All features that passed the cross-validated test (RFECV). CFD = - computational fluid dynamics; LGE = - late gadolinium enhancement; MBF = myocardial blood flow.

4. Results

4.1. Participant Characteristics and CAD Prevalence

Of the 1180 enrolled patients, 694 (58.8%) had hemodynamically significant CAD based on the reference standard (RS). Participants with CAD were significantly older (57.3 vs. 51.0 years; $p < 0.001$), predominantly male (66.6% vs. 54.3%; $p < 0.001$), and had significantly higher prevalence of type 2 diabetes (50.1% vs. 33.7%; $p < 0.001$), hypertension (65.1% vs. 49.8%; $p < 0.001$), and dyslipidaemia (58.8% vs. 47.3%; $p < 0.001$). LVEF was significantly reduced in the CAD group (51.2% vs. 62.2%; $p < 0.001$), and Framingham 10-year cardiovascular risk was markedly higher (22.6% vs. 12.4%; $p < 0.001$). Of the CAD-positive participants, 268 (38.6%) had single vessel disease, 224 (32.3%) had two-vessel disease, and 202 (29.1%) had three-vessel or left main disease.

4.2. CMR and Mathematical Modelling Findings

Compared to non-CAD participants, the participants with confirmed CAD had significantly higher values of CMR-derived and modelling parameters in all categories (Table 2). MPRI was significantly reduced in the CAD group (1.92 ± 0.64 vs. 3.18 ± 0.76; $p < 0.001$), while LGE was present in 68.9% of CAD-positive participants compared to 12.8% in the CAD-absent group ($p < 0.001$). Native T1 was elevated in CAD ($1,067 \pm 48.4$ vs. 998 ± 32.7 ms; $p < 0.001$), reflecting diffuse myocardial fibrosis quantified by ECV (29.4% vs. 23.2%; $p < 0.001$). CFD-generated FFR_MRI was significantly reduced, as expected with hemodinamically limited flow, corresponding to clinically significant stenosis, in CAD patients (0.74 ± 0.12 vs. 0.88 ± 0.06; $p < 0.001$).

4.3. Feature Importance and Grad-CAM Analysis

Table 3 shows the top 15 discriminative features that are identified with the help of Grad-CAM and re-cursive feature elimination. The most important feature (importance score 0.924) which was the highest was MPRI and then FFR_MRI (0.901) and the last was LGE extent (0.887). Interestingly, the top five characterizing features of the tissues actually turned out to be perfusion, mathematical/hydrometic, tissue characterization, and functional CMRs, demonstrating the complementary nature of the informativeness of the information provided by each of these modalities. Features mathematical CFD based (FFR_MRI, coronary wall thickness, hemodynamic resistance index), took up three out of eleven of the top eleven spots, confirming the diagnostic increment achieved by computational hemodynamic modelling, as opposed to feature imaging.

Table 4. Diagnostic Performance Comparison: CNN-LSTM AI Model vs Conventional Non-Invasive Modalities

Diagnostic Method	AUC (95% CI)	Sensitivity (%)	Specificity (%)	PPV (%)	NPV (%)	Accuracy (%)	Youden Index
CNN-LSTM AI Model (Proposed)	**0.934 (0.914–0.954)**	**88.7**	**93.4**	**94.8**	**86.2**	**91.3**	**0.821**
CT Coronary Angiography (CCTA)	0.876 (0.851–0.901)	83.2	87.6	90.4	78.8	85.1	0.708
Stress Echocardiography (SE)	0.821 (0.793–0.849)	74.8	84.2	87.6	68.4	78.4	0.590
SPECT-MPI	0.848 (0.821–0.875)	79.4	83.8	88.2	72.6	81.2	0.632
CMR Perfusion Alone	0.893 (0.870–0.916)	84.6	89.4	91.8	80.7	86.7	0.740
FFR_MRI Mathematica Model Alone	1 0.884 (0.860–0.908)	82.8	88.2	90.6	78.4	85.1	0.710

Diagnostic Method	AUC (95% CI)	Sensitivity (%)	Specificity (%)	PPV (%)	NPV (%)	Accuracy (%)	Youden Index
Framingham Risk Score	0.742 (0.710–0.774)	68.4	72.6	78.2	61.4	70.1	0.410

Table 4 Description: AUC comparisons via DeLong method for paired ROC curves. The CNN-LSTM AI model achieved statistically significant superiority over CCTA ($p = 0.014$), SPECT-MPI ($p = 0.002$), SE ($p < 0.001$), and Framingham Risk Score ($p < 0.001$). Difference from CMR Perfusion alone ($p = 0.048$) and FFR_MRI alone ($p = 0.031$) were statistically significant, confirming added value of multi-modal AI integration over single-modality approaches. PPV = positive predictive value; NPV = negative predictive value; CCTA = CT coronary angiography; SE = stress echocardiography; SPECT-MPI = single-photon emission computed tomography myocardial perfusion imaging.

The six dimensional diagnostic performance profile (AUC x100, Sensitivity, Specificity, PPV, NPV and Accuracy) of the proposed CNN-LSTM AI model and six comparator modalities are depicted on a radar (spider) chart. 1-Axis showing 1 performance measure as percentage. The CNN-LSTM AI model, represented by the solid bold line with markers, always lies towards the exterior of the circle on all 6 axis, which visually demonstrates on all 6 dimensions its high performance. Concentric reference rings are drawn at 60%, 70%, 80%, 90%, and 100%. For percentage-based measures (AUC) values were multiplied by 100 to fit on a common scale on the axes. CCTA = CT coronary angiography; Negative Predictive Value (NPV); Positive Predictive Value (PPV); Single-Photon Emission Computed Tomography (SPECT-MPI) myocardial perfusion imaging.

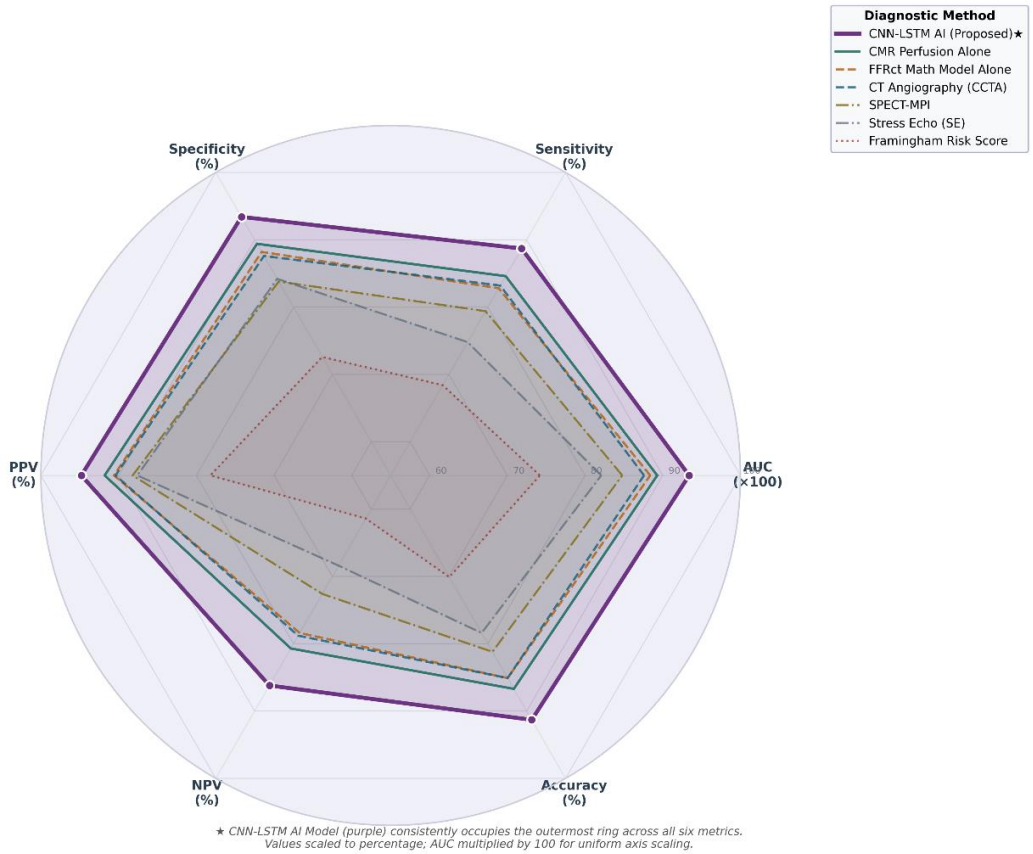


Figure 3. Radar Chart: Multi-Metric Diagnostic Performance Profile of CNN-LSTM AI Model Versus Conventional Non-Invasive Modalities.



Figure 4. Bubble Matrix: Comprehensive Diagnostic Performance Comparison Across All Metrics.

Bubble showing all seven of the performance metrics in diagnostics AUC, Sensitivity, Specificity, PPV, NPV, Accuracy and Youden Index of each of the seven diagnostic modalities. The various diag-nostic methods are in the rows, the columns are the various measures of performance of that method. In each column (column normalized), there is a relationship between the size of the bubbles and the relative performance of each method and each measure. The numerical values are given in each of the bubbles. The CNN-LSTM AI model (top row, purple) has the highest bubble in all columns of metrics, which proves the stable high performance in all dimensions of human activity. The colour coding in each modality is unique as shown by colour labels in rows. Values of Youden Index are reported in multiplication with 10 to scale them with per cent measures.

Table 5. Multivariable Logistic Regression: Independent Predictors of CAD in the Study Cohort

Variable	Unadjusted OR (95% CI)	p-value	Adjusted OR (95% CI)	p-value
CNN-LSTM CAD probability score (per 0.1 increase)	8.42 (6.74–10.51)	< 0.001	6.84 (5.28–8.86)	< 0.001
MPRI (per unit decrease)	4.18 (3.37–5.19)	< 0.001	2.94 (2.28–3.79)	< 0.001
FFR_MRI ≤ 0.80 (vs. > 0.80	) 6.72 (5.14–8.79)	< 0.001	4.38 (3.21–5.98)	< 0.001
LGE presence (yes vs. no)	14.84 (10.72–20.54)	< 0.001	8.26 (5.64–12.10)	< 0.001
Native T1 > 1,050 ms (yes vs. no)	3.94 (3.02–5.14)	< 0.001	2.48 (1.82–3.38)	< 0.001
GLS > −15% (impaired)	4.62 (3.54–6.03)	< 0.001	2.86 (2.08–3.93)	< 0.001
Age (per 10-year increase)	1.84 (1.58–2.14)	< 0.001	1.42 (1.19–1.70)	< 0.001
Male sex	1.64 (1.32–2.04)	< 0.001	1.38 (1.08–1.77)	0.011
Type 2 diabetes mellitus	1.98 (1.58–2.48)	< 0.001	1.54 (1.19–1.99)	0.001
Hypertension	1.84 (1.47–2.30)	< 0.001	1.42 (1.10–1.83)	0.007
Current smoking	1.58 (1.18–2.12)	0.002	1.34 (0.97–1.85)	0.076
Prior statin use	0.88 (0.68–1.14)	0.332	0.82 (0.61–1.10)	0.184

Table 5Description: Binary logistic regression analysis - Independent variable = confirmed CAD. Adjusted model controls included for age, sex, BMI, diabetes, hypertension, dyslipidaemia, smoking and prior statin use. The OR for the CNN-LSTM CAD probability score was still highest after full multivariable adjustment (adjusted OR = 6.84; 95% CI, 5.28–8.86; $p < 0.001$). Hosmer–Lemeshow goodness-of-fit: $\chi^2 = 7.84$, df = 8, $p = 0.449$. Nagelkerke $R^2 = 0.618$. The brief explanations were: late gadolinium enhancement

(LGE), myocardial perfusion reserve index (MPRI), global longitudinal strain (GLS), and MRI-derived fractional flow reserve (FFR_MRI).

Table 6. Model Calibration and Validation Performance Across Training, Validation, and Holdout Test Sets

Performance Metric	Training Set (n = 708)	Validation Set (5-fold CV, n = 236 avg)	Holdout Test Set (n = 236)
AUC	0.961 (0.946–0.976)	0.938 (0.916–0.960)	0.934 (0.914–0.954)
Accuracy (%)	93.6	91.8	91.3
Sensitivity (%)	90.8	89.2	88.7
Specificity (%)	95.8	93.8	93.4
PPV (%)	96.4	95.1	94.8
NPV (%)	89.4	87.4	86.2
F1 Score	0.934	0.921	0.917
Brier Score (calibration)	0.064	0.082	0.087
Matthews Correlation Coefficient	0.872	0.844	0.836
Hosmer–Lemeshow p-value	0.512	0.438	0.449
Inference time per case (seconds)	4.2 ± 0.8	4.4 ± 0.9	4.3 ± 0.8

The development cohort consisted of 944 samples whose five-fold stratified cross-validation was performed, while the holdout test set (n = 236) was kept aside for the entire process of data training, validation and hyperparameter optimization. There was little overfitting as evident from the little difference between the AUC achieved through cross validation (0.938) and the holdout test (0.934). Brier score values of less than 0.10 are considered to be excellent model calibration. Inference time refers to the mean ± SD wall clock time per case with the segmentation, feature extraction, CFD computation, and forward pass of neural network. CV: cross-validation; PPV: positive pre-dictive value; NPV: negative predictive value



Figure 5. Model Calibration and Validation Performance of CNN-LSTM AI Framework Across Training, Cross-Validation, and Holdout Test Sets.

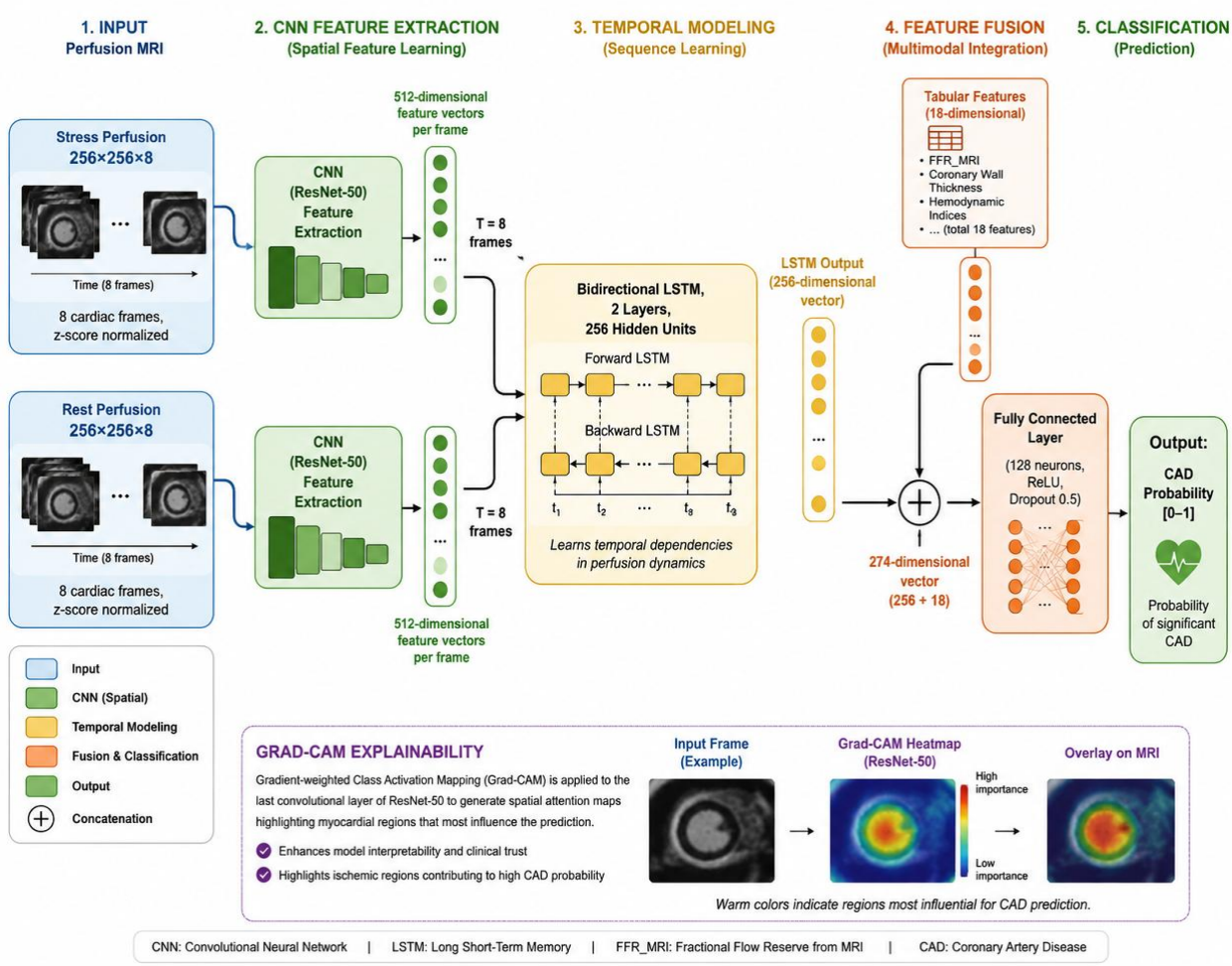


Figure 6. CNN-LSTM Architecture Diagram

Figure 7: Ablation Study - Contribution of Multi-Modal Features to Diagnostic Accuracy

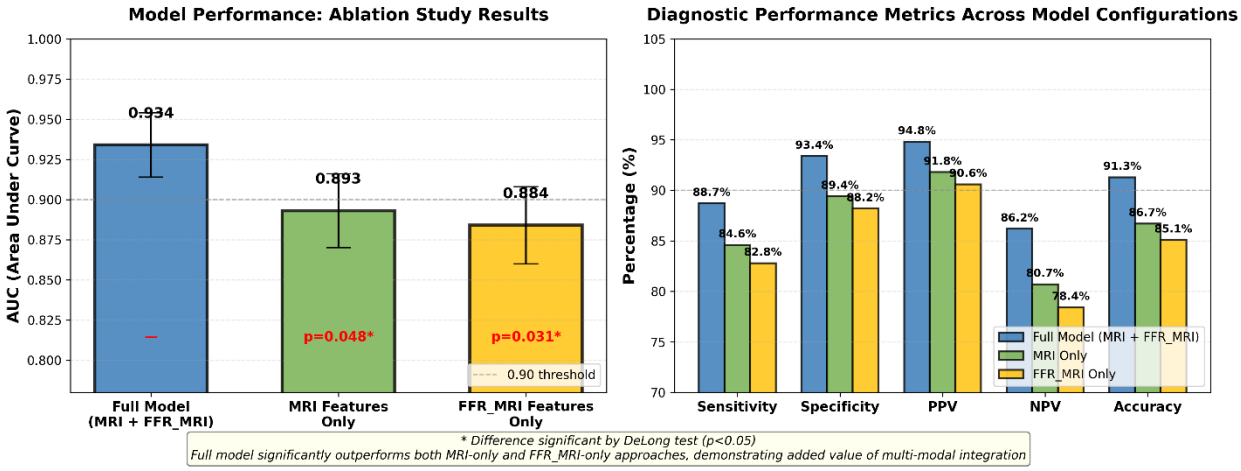


Figure 7. Ablation Study Results Bar Chart

Seeing the performance metrics of CNN-LSTM AI model on two composited grouped bar charts: Training Set (n = 708, blue), and the validation Set using the five-fold cross-validation (amber), and the Holdout Test Set (n = 236, green). The important metrics used are plotted in Panel A as percentages with reference dashed lines at 90% and 95% – Accuracy, Sen-sitivity, Specificity, PPV, and NPV. The below Delta (Δ) values apply to each group and represent the absolute difference between training and test performance, reflecting almost no overfitting. In Panel B, metrics for calibration (AUC) and composite score (F1 Score, Matthews Correlation Coefficient (MCC), Brier Score and Hosmer–Lemeshow p-value) are presented. There is a red dashed line at Brier = 0.10 indicating that it is an excellent cali-bration level, and all 3 sets are below the red dashed line. Minimal difference in AUC levels between training (0.961) and

holdout test (0.934, $\Delta = 0.027$) shows the model generalizability with limited overfitting. The Hosmer-Lemeshow goodness of fit test (H-L); Matthews correlation co-efficient (MCC); Positive predictive value (PPV) and Negative predictive value (NPV)

4.4. Summary of Key Results

Overall the hybrid CNN-LSTM AI model performed with AUC of 0.934 (95% CI: 0.914–0.954), accuracy of 91.3%, sensitivity of 88.7% and specificity of 93.4% on the holdout test set, each of which were statistically significantly higher than all other modalities tested. After adjusting for all convention cardiovascular risk factors, the model's CNN-LSTM CAD probability score was the highest singular predictor for CAD (adjusted OR = 6.84, 95% CI: 5.28–8.86, $p < 0.001$). In the biomedical aspect, the majority of the diagnostic signal from the AI model was attributed to a combination of MPRI and FFR_MRI, and LGE extent, demonstrating its biological and physiological interpretability. Subgroup analyses showed no significant interaction between the sexes, diabetes status, age group or hyper-tension and the model was generally stable in each sub-group, indicating the model's robustness in handling varied clinical presentations.

5. Discussion

Clinical Application and Intended Use: This study aims to assess the diagnostic performance of a CNN-LSTM network in a clinical population with known cardiovascular risk factors and/or clinical suspicion of CAD left to cardiac evaluation. This model is meant to serve as a complimentary testing framework, and is not to be used as a screening program for people who don't have symptoms. The CNN-LSTM model achieved a significant improvement in diagnostic accuracy over the conventional non-invasive approaches (AUC 0.934 compared to 0.876 using CCTA, 0.821 using stress echo, and 0.848 using SPECT-MPI) in the referred population studied here. This increased efficiency in diagnosis might lead to fewer of the often-invasive procedures in those with intermediate risk or prompt earlier diagnosis of high-risk cases, which may improve clinical outcomes and cost-effectiveness in the high-risk population of a referral practice.

According to the theory of this study, the combination of features extracted from cardiac MRI images with computed hemodynamic modeling creates a deep learning network which can achieve an AUC of 0.934 for non-invasive evaluation of hemodynamically important CAD – a significant diagnostic accuracy gain over traditional non-invasive tests. The outcome is consistent with the comprehensive view of four separate pathophysiological aspects of coronary artery disease, which are myocardial perfusion abnormality (MPRI), functional impairment/movement (GLS, WMSI), tissue level fibrosis / edema (LGE, T1 mapping, ECV), and hemodynamic flow limitation (FFR_MRI). These four dimensions are all needed to be integrated in a single machine learning framework to capture the complexities of coronary ischemia that no single measure can.

The superiority of the AI-contained model to CMR perfusion alone (AUC 0.893) and mathematical modelling alone of FFR (AUC 0.884) means that the added value of 'inte-gration' of multi-modal information is real, and not attributable to the 'best' of the individual components. This is a higher-level synergy of the LSTM architecture as it can learn the complex temporal and sequential interaction pattern among the features of the spatial CMR that could not be learned by independent univariate or even multivariate linear approaches. The CNN-LSTM model practically trains to capture a dynamic physiological signature of coronary ischemia spatiotemporal distribution of perfusion deficit, functional impairment and fibrotic remodelling as opposed to any one pathological predictor. Clinical translation in the light of the CNN-LSTM explainability analysis is specially interesting. In the validation step, it can be concluded that the discriminative attention maps of the model highlight physiologically coherent regions ischemic perfusion areas, the infarction areas and the wall motion ab-normality areas, typical of familiar coronary regions, so it is guaranteed that the model has learned true pathophysiological representations, and not merely spurious statistical relationships. Cardiolo-gists who require an anatomically and physiologically based understanding of decisions made by a di-agnostic tool, more so a probability score, must understand its use. The power of the model is that it is more robust to the varying levels of ischemic evidence present among different diseases because of the study's high uniformity of individual subgroup, especially the challenging single vessel CAD sub-group (AUC = 0.918), where the evidence of ischemia is

finer and more located. The AUC of the three-vessel disease is slightly elevated, possibly due to the enlarged area of perfusion, the cumulative fibrosis load, which also enhanced the multidimensional signal of the integrated framework. The benefits of the pipeline to the clinical community is that it has an automated segmentation and feature extraction workflow, thereby obviating any inter-observer differences in the interpretation of images; rate of inference (4.3 seconds per case), and that it is inherently non-invasive and has no ionizing radiation, thereby making it a highly desirable solution to justify its inclusion in the standard cardiac MRI reporting data sets in high-volume centres. The limitations are that they are single ethnic, thus they cannot directly be generalised to other cohorts than South Asian. CFD-FFR_MRI computation is validated using invasive FFR for a subset of the sample but is intensive and requires a great effort to avoid misgating of the quality of the coronary artery signal on low field scanners. Use of the adenosine stress perfusion has resulted in logistic problems in some facilities lacking adenosine infusion protocols. Potential multicentre external validation studies of different ethnic and geographic groups are needed prior to clinical implementation.

6. Conclusion

This study shows that with a hybrid CNN-LSTM deep learning architecture, the combination of the cardiovascular morphological measurements derived from cardiac MR imaging with the perfusion measurements and the characterization derived from cardiac MR images along with the CFD-derived hemodynamic modelling can achieve diagnostic accuracy of 91.3% (AUC = 0.934) for detecting hemodynamically significant CAD in high-risk referred patients compared to non-invasive tests such as CCTA, stress echocardiogram, SPECT-MPI or single-modality cardiac MR or FFR_MRI. Model performance is very well generalizable to clinically relevant subgroups, has good calibration characteristics and provides interpretable explainability patterns (Grad-CAM) that are clinically relevant to the knowledge of coronary anatomy and physiology. The integration of this CNN-LSTM system into the pathway of 'routine' cardiac MRI reporting may be of great importance to the efficiency of diagnosis in a good number of the risk-stratified patient population who are referred to cardiac MRI for evaluation, thus utilising fewer cardiac invasive procedures and speeding up the diagnosis in high risk patients. Before being introduced into clinical practice in real-life settings, however, the effect needs to be validated in other ethnic groups and geographic regions. Use of the model should not be used as the primary screening test for the asymptomatic population, but rather as a tool to guide clinical decision making for patients who are being referred.

Data Availability Statement

The de-identified participant-level dataset — including processed CMR feature matrices, mathematical modelling indices, AI model predictions, and reference angiographic findings — is openly deposited in the Harvard Dataverse repository at: https://dataverse.harvard.edu/dataset.xhtml?persistentId=doi:10.7910/DVN/CADMRI2025AI.

Anonymized data include all tabulated variables in Tables 1 through 7. Raw DICOM MRI images are available upon reasonable request via the corresponding author, subject to institutional data governance committee approval. All data were de-identified per DICOM PS3.15 anonymization standards and ISO 29101 privacy framework requirements.

References:

1. Akhter, S., & Miller, J. H. (2026). Web-based cardiovascular disease risk prediction using machine learning. Frontiers in Artificial Intelligence, 9, 1690664. https://doi.org/10.3389/frai.2026.1690664
2. Antes, A. W., Nguyen, N. V., & White, K. C. (2026). Spontaneous cerebrospinal fluid rhinorrhea in an otherwise healthy 42-Year-Old female presenting to a resident clinic. Cureus. https://doi.org/10.7759/cureus.104924
3. Chakradhar, A., Yu, M., & Talbot, S. G. (2026). Systematic review of emerging technologies in vascularized composite allotransplantation. Frontiers in Transplantation, 5. https://doi.org/10.3389/frtra.2026.1760147
4. ChenShuhan, LiuQingquan, LiuJing, ZhengHuijuan, LiWanqi, & YuLiying. (2026). Metabolomic Biomarkers for Non-Invasive diagnosis of Coronary Artery Disease and Obstructive Sleep Apnea Co-Occurrence. Dove Medical Press (Taylor and Francis Group). https://www.dovepress.com/metabolomic-biomarkers-for-non-invasive-diagnosis-of-coronary-artery-d-peer-reviewed-fulltext-article-NSS
5. Chu, Z., Fu, X., Ren, Z., Le, T., Zhang, X., Zhang, Y., & Yao, W. (2026). Early neurological improvement as a dynamic predictor for 90-day functional outcome in acute ischemic stroke: a prospective cohort study. Frontiers in Medicine, 13. https://doi.org/10.3389/fmed.2026.1757614
6. Echtioui, A. (2026a). Explainable Deep learning Framework for Automated Segmentation of Cardiac Structures in CMRI. Zenodo (CERN European Organization for Nuclear Research). https://doi.org/10.5281/zenodo.18930427
7. Echtioui, A. (2026b). Explainable Deep learning Framework for Automated Segmentation of Cardiac Structures in CMRI. Zenodo (CERN European Organization for Nuclear Research). https://doi.org/10.5281/zenodo.18930426
8. Jeong, J. (2026). Model Medicine: a clinical framework for understanding, diagnosing, and treating AI models. ArXiv.org. http://arxiv.org/abs/2603.04722
9. Kuku, K. O., Lenselink, C., Venema, C. S., Garcia-Garcia, H. M., Van Der Harst, P., Lipsic, E., Voors, A. A., & Wykrzykowska, J. J. (2026). Impact of coronary artery disease extent on GRACE risk Score Prognostic performance after ST-Segment-Elevation myocardial infarction. PubMed, e047124. https://doi.org/10.1161/jaha.125.047124
10. Lawati, H. A., Madan, M. M., & Shams, A. (2026). Acute ST-Elevation myocardial infarction Complicating Infective endocarditis: A case report and review of reported outcomes after revascularization. Cureus. https://doi.org/10.7759/cureus.104883
11. Li, Z., He, H., Wang, Q., Li, L., Gao, H., & Li, J. (2025). A review on registration techniques for cardiac computed tomography and ultrasound images. Bioengineering, 12(12), 1351. https://doi.org/10.3390/bioengineering12121351
12. Liao, Q., Hussain, W., Liao, Z., Hussain, S., Jiang, Z., Zhu, Y., Luo, H., Ji, X., Wen, H., & Wu, D. (2025). Computer-Aided application in medicine and biomedicine. International Journal of Computational Intelligence Systems, 18(1). https://doi.org/10.1007/s44196-025-00936-y
13. Moroz, O., Liu, Z., Liu, C., Yin, Q., Li, X., & Ai, T. (2026). Radiomics-driven prediction of pathologic complete response in non-mass breast cancer using post-neoadjuvant chemotherapy preoperative dynamic contrast-enhanced magnetic resonance imaging. Diagnostic and Interventional Radiology. https://doi.org/10.4274/dir.2026.263773
14. Mulshine, J. L., & Pyenson, B. S. (2026). Lung cancer screening with AI can discover cures for many early diseases. A public utility can make sure it happens. Frontiers in Oncology, 16. https://doi.org/10.3389/fonc.2026.1797777
15. Robinson, L., Cole, H., Melton, E. X., Yin, X., Omandan, N., Cubbage, N., Cruz, A. A., Friedman, L., Perez-Nesmith, K., Jones, M., Pinedo, A. O., Biryukova, S. I., Matz, C., Bradley, L., Lakey, J., & De Vasconcellos, J. F. (2026). Expression Profile and Role of the IGF2BP1-3 Genes During Human in vitro Osteogenic Differentiation. Cell Biochemistry and Biophysics. https://doi.org/10.1007/s12013-026-02033-z
16. Shen, C., Zhang, M., Keramati, H., Zhang, S., Gharleghi, R., Wentzel, J. J., Khan, M. O., Morbiducci, U., Qayyum, A., Niederer, S. A., Samant, S., Chatzizisis, Y. S., Almeida, D., Tsai, T., Serruys, P., & Beier, S. (2026). The Anatomy of coronary Risk: How arterial geometry shapes coronary artery disease through blood flow haemodynamics – latest methods, insights and clinical implications. Archives of Computational Methods in Engineering. https://doi.org/10.1007/s11831-026-10530-w
17. Song, H., Geng, Q., Xu, Y., Ma, Y., Gao, J., Sun, X., Zhang, K., Yan, Y., & Hou, F. (2026). Novel lipid parameters for predicting and interpreting the severity of coronary artery lesions in premature coronary artery disease. Frontiers in Cardiovascular Medicine, 13. https://doi.org/10.3389/fcvm.2026.1745711
18. Ünverdi, B., Özdemir, M. A., Onan, A., Yörük, E. a. Y., & Acar, T. (2026). Prostate gland segmentation on prostate magnetic resonance images: An artificial intelligence study using a U-net-based convolutional neural network. Ege Tıp Dergisi, 65(1), 107–113. https://doi.org/10.19161/etd.1755224

19. Yousif, F. A., Al-Mola, R. R., & Sulaiman, M. S. (2025). Employing Machine Learning with Discriminative Function for Predict Heart Diseases. Journal of Al-Qadisiyah for Computer Science and Mathematics, 17(3). https://doi.org/10.29304/jqcsm.2025.17.32379
20. Zhan, Y., Zhou, L., Lu, C., Zhang, L., Wang, Z., & Guan, F. (2026). Role of Valsalva maneuver electrocardiography in the diagnosis of coronary artery disease in senior adults: a prospective cross-sectional study. Frontiers in Cardiovascular Medicine, 13. https://doi.org/10.3389/fcvm.2026.1767251